Materials Today Communications 36 (2023) 106669

Contents lists available at ScienceDirect

Materials Today Communications

journal homepage: www.elsevier.com/locate/mtcomm

Vapor-induced flow and its impact on powder entrainment in laser powder bed fusion

Zhiyong Li [a,c,g], Gang Yu [a,b,d], Xiuli He [a,d,*], Zhengtao Gan [e,f,**], Wing Kam Liu [e,***]

[a] Institute of Mechanics, Chinese Academy of Sciences, Beijing 100190, China
[b] Center of Materials Science and Optoelectronics Engineering, University of Chinese Academy of Sciences, Beijing 100049, China
[c] Welding and Additive Manufacturing Centre, Cranfield University, Cranfield, Bedfordshire, MK43 0AL, United Kingdom
[d] School of Engineering Science, University of Chinese Academy of Sciences, Beijing 100049, China
[e] Department of Mechanical Engineering, Northwestern University, Evanston 60201, USA
[f] Department of Aerospace and Mechanical Engineering, The University of Texas at El Paso, El Paso 79968, USA
[g] Visiting scholar from 2019 to 2021. Department of Mechanical Engineering, Northwestern University, Evanston 60201, USA

ARTICLE INFO

Keywords:
Numerical modeling
Powder spattering and denudation
3D printing and additive manufacturing
Vapor plume flow
Vapor-induced gas flow

ABSTRACT

A 2D axisymmetric transient Thermal-Fluid-Evaporation model coupled with melt pool dynamics and gas kinetics is developed to study the formation mechanisms of vapor-induced flow and the resulting powder entrainment in powder bed fusion using laser beam (PBF-LB) for 316 L powders. The interactions between keyhole formation inside the melt pool, vapor plume flow, and vapor-induced shielding gas flow are investigated. Vapor plume flow results in powder spattering with much higher speed, while vapor-induced gas flow significantly contributes to powder denudation with lower speed. It is also reported that powder spattering is stronger in 1 atm argon than that in 1 atm helium because the drag force for spattering is 2.72 times larger in 1 atm argon, but powder denudation becomes greater in 1 atm helium as the ratio of drag force for denudation in 1 atm argon to that in 1 atm helium is only 0.582. Furthermore, the vapor plume results in more spatters with the decrease of ambient pressure from 1 atm to 0.05 atm in argon because the plume is diluted faster with a twofold wider plume head and the two times higher peak velocity as a result of the pressure drop-induced significant reduction of viscosity restriction. A larger divergency angle in 0.05 atm argon is also recorded at the same time for the weaker restriction and faster dilution. In combination with in-situ observations, the proposed model provides insights into the vapor-induced flow, and its impact on powder entrainment under different gas types and ambient pressures.

1. Introduction

Powder bed fusion using a laser beam (PBF-LB), also called selective laser melting (SLM), is one of the most promising metal additive manufacturing processes, attracting numerous practitioners from automobile, aerospace, and healthcare. PBF-LB provides advantages in flexible design, high manufacturing efficiency, and superior structuring performance [1–3]. However, widespread acceptance by the industrial community is still limited by the quality and uncertainty arising from process-induced defects such as pores and cracks. Among many underlying causes of such defects, unexpected powder entrainment has been identified as one of the significant reasons [4–6]. The so-called powder entrainment can be classified as powder spattering moving away from the melt pool at a higher speed and powder denudation that moves towards the melt pool along the surface of the powder layer at a much smaller speed.

Optical observation through different imaging technologies is capable of providing reliable online details of powder entrainment in PBF-LB [7–12]. Accordingly, these imaging techniques can also provide the quantitative measurement of spatters and denudated powders. To directly observe and analyze the transient dynamics of the powder entrainment in PBF-LB, Guo et al. [7] used in-situ high-speed, high-energy X-ray imaging facilities in Argonne National Laboratory (ANL), and Bidare et al. [8] conducted Schlieren imaging technology

---

* Corresponding author at: Institute of Mechanics, Chinese Academy of Sciences, Beijing 100190, China.
** Corresponding author at: Department of Mechanical Engineering, Northwestern University, Evanston 60201, USA.
*** Corresponding author.
E-mail addresses: xlhe@imech.ac.cn (X. He), zgan@utep.edu (Z. Gan), w-liu@northwestern.edu (W.K. Liu).

https://doi.org/10.1016/j.mtcomm.2023.106669
Received 18 April 2023; Received in revised form 7 July 2023; Accepted 13 July 2023

integrated with PBF-LB device. Other technologies, including fast camera, optical pyrometer, and infrared thermography, have also been used to observe the powder entrainment in PBF-LB [9–12]. Despite the gained insights, the experimental methods are expensive in comparison with numerical modeling, which can also provide predictive approaches for the printing process.

Modeling and simulation have also been used to obtain high-fidelity features about melt pool dynamics, vapor-induced flow, and powder entrainment to reveal insights [13,14]. For example, Matthews et al. [15] established a powder-scale finite element model to study the powder denudation near a laser scan path as a function of processing parameters and gas pressure. Chen et al. [16] developed a multiphase flow model to analyze the effects of vapor-induced flow on powder spattering and denudation, in which the melt pool dynamics were not considered, and the vapor plume flow was simplified as a velocity inlet. Bidare et al. [17] also proposed a multi-physics model to quantify the vapor plume flow observed by Schlieren imaging. Similarly, the vapor plume, which jets into the shielding gas at high speed, is assumed as multi-component plasma without considering melt pool dynamics. From the obtained insights into modeling [18–20], the lack of melt pool dynamics results in the temperature data with larger error and not capable of obtaining the physical details of fluid flow and evaporation of the melt pool. Thus, lower modeling accuracy and lack of physical information are expected to be caused by the simplified energy and momentum boundaries in [16] and [17]. Besides, this simplification leads to the challenges of describing the vapor-induced flow.

The ambient pressure has been demonstrated a non-negligible factor for powder entrainment [7]. Although the vapor-induced flow is not directly recorded in [7], it was experimentally confirmed that the total number of spattered powders depends on the initial pressure of the atmosphere. In addition, the influence of gas type has also drawn much attention [21–23]. Pure argon, and pure helium, as well as the mixed gas of argon and helium, are widely used as shielding gas in the PBF-LB process. Baehr et al. [21] concluded that the vapor plume and total incandescent spatters are both reduced when helium is contained in shielding. Pauzon et al. [22,23] also found that by using He and Ar-He mixtures, the hot spatters are obviously reduced because the vapor plume is rapidly away from the laser spot. However, the causal relations between melt pool dynamics, vapor-induced flow, and powder entrainment are not well revealed due to the restrictions from observation technologies.

To fill these gaps, a coupled melt pool dynamics and gas kinetics computational model for PBF-LB of 316 L is developed to explore the physical mechanisms of vapor-induced flow and its impact on powder entrainment. This model is initially validated by experimental observation from the literature. Next, it is set up to investigate shielding gas's impact by coupling vapor plume flow and vapor-induced gas flow for 1 atm argon and 1 atm helium, respectively. Furthermore, the role of environmental pressure on vapor-induced flow and the resulting powder entrainment is continuously studied in argon. Finally, a mechanism of powder entrainment considering the variations of shielding gas types and environmental pressures is proposed. Validated by experiments, the obtained hypothesis could help design potential approaches to mitigate the powder entrainment-induced defects and improve the printing quality.

2. Numerical procedure

A directly coupled 2D axisymmetric transient Thermal-Fluid-Evaporation model is proposed to simulate the melt pool dynamics and vapor-induced flow during PBF-LB of 316 L powders. For the melt pool behavior, heat transfer and incompressible flow are simulated by solving the equations of conservation of mass, momentum, and energy with the keyhole surface captured by the Arbitrary-Lagrangian-Eulerian (ALE) method. For the coupled laser-induced vapor plume flow and vapor-induced gas flow with compressibility in shielding gas, the equation describing vapor plume dilution is also considered together with the mass, momentum, and energy equations. PARDISO solver is used to solve the fully-coupled equations with the maximum time step of 1 ms. Details of the model development, including model geometry, mesh discretization, governing equations, and boundary conditions, are described as follows.

2.1. General description of vapor-induced flow and powder entrainment

For the visualization given in Fig. 1, vapor plume flow is plotted by pink trapezia, and the silhouette of trapezia represents its acting area in which powders can be heated and driven to move at high speed. Meanwhile, the acting area of vapor-induced gas flow is depicted by a black dotted line with arrows. Blue circles are the initial powder layer, green circles are denudated powders, and red circles denote spatters. A high-power density laser beam melts powders after a short time of irradiation. The high-speed vapor plume induced by laser, i.e., the vapor materials in the gas phase, is formed together with melt pool. Vapor-induced gas flow is driven by the shear stress between vapor plume and shielding gas (helium and argon in this study). Dragged by the vapor plume flow and vapor-induced gas flow, the resulting powder entrainment can be classified as powder spattering and denudation according to the powder moving direction and moving speed. It is noted that spatters move from the top upwards away from the melt pool, while denudated powders approach the melt pool near the top of the powder layer. Spatter here actually denotes the spattered powders that move away from the melt pool during PBF-LB.

On the other hand, spatters' speed is much higher than denudated powders. Thus, spattered powders travel a longer distance at the same time interval. Connecting the simulation results from the model along with high-resolution observations from published works, the fundamental mechanism of powder entrainment (i.e., powder spattering and denudation) can be analyzed based on the fact that the driving force for powder entrainment comes from vapor-induced flow (i.e., vapor plume flow and vapor-induced gas flow).

2.2. Material properties and numerical constants

This work simulates melt pool dynamics, vapor plume flow, and vapor-induced gas flow to analyze the resulting powder spattering and denudation during PBF-LB of 316 L powders. Thermal-physical properties and numerical constants used in modeling are listed in Table 1.

2.3. Major assumption

In the present model, vapor-induced gas flow is only resulted from the shear stress between high-speed vapor plume and shielding gas, and the initial flow of shielding gas is not considered for simplification. The

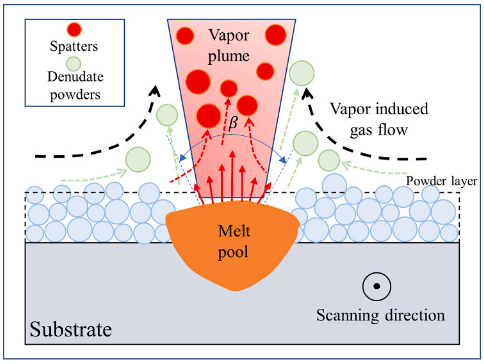

Fig. 1. Schematic sketch of the vapor plume flow, vapor-induced gas flow (helium, argon), powder spattering and denudation in laser powder bed fusion (PBF-LB). Scan direction is going into the plane.

Table 1
Thermal-physical properties and numerical constants used in simulation.

Properties for IN625 [17]		
C_p	Specific heat (J/kg/K)	680
K	Thermal conductivity (W/m/K)	26.9
L_m/L_V	Enthalpy of melting/evaporation (kJ/kg)	270/6294
M	Molar mass (g/mol)	59.47
R_λ	Reflectivity	0.7
T_s/T_l	Solidus/liquidus temperature (K)	1533/1609
T_V	Boiling temperature (K)	3190
γ	Thermocapillary coefficient (N/m/K)	-1.1×10^{-4}
μ	Dynamic viscosity (Pa·s)	2.0×10^{-3}
ρ	Density (kg/m^3)	7886
σ	Surface tension (N/m)	1.84
Properties for 316L [24]		
C_p	Specific heat (J/kg/K)	760
K	Thermal conductivity (W/m/K)	35.0
L_m/L_V	Enthalpy of melting/evaporation (kJ/kg)	247/6520
M	Molar mass (g/mol)	56
R_λ	Reflectivity	0.7
T_s/T_l	Solidus/liquidus temperature (K)	1697/1727
T_V	Boiling temperature (K)	3100
γ	Thermocapillary coefficient (N/m/K)	-4.3×10^{-4}
μ	Dynamic viscosity (Pa·s)	6.0×10^{-3}
ρ	Density (kg/m^3)	7200
σ	Surface tension (N/m)	1.7
Properties for argon [25]		
C_p	Specific heat (J/kg/K)	520
K	Thermal conductivity (W/m/K)	1.7×10^{-2}
M	Molar mass (g/mol)	39.95
μ	Dynamic viscosity (Pa·s)	2.26×10^{-5}
Properties for helium [25]		
C_p	Specific heat (J/kg/K)	5193
K	Thermal conductivity (W/m/K)	1.55×10^{-1}
M	Molar mass (g/mol)	4.00
μ	Dynamic viscosity (Pa·s)	1.98×10^{-5}
Numerical constants		
a_1/b_1	Ablation rate constants	$1.05 \times 10^{-6}/1.01 \times 10^{-2}$
c_1/d_1	Ablation rate constants	$32.71/-3.57 \times 10^4$
a_2/b_2	Surface pressure constants	$1.41 \times 10^{-3}/-13.51$
c_2/d_2	Surface pressure constants	$4.34 \times 10^{-4}/-4.66 \times 10^{-7}$
D	Diffusion coefficient (m^2/s)	2×10^{-5}
T_L/T_H	Vaporization thresholds (K)	3200/3698

Table 2
Physics field, boundary condition, and the corresponding location in model geometry.

Domain	Physics field	Boundary condition	Boundary
Substrate domain	Heat transfer	Laser irradiation	B.E.
		Convection	B.E. A.D. D.E.
		Radiation	B.E.
	Fluid flow	Stress balance	B.E.
		No-slip	A.D. D.E.
	ALE	Prescribed deformation	A.D. D.E.
		Free deformation	B.E.
Gas domain	Heat transfer	Thermal continuity	B.E.
		Insulation	E.F. C.F.
	Fluid flow	Velocity inlet	B.E.
		Ambient pressure	E.F. C.F.
	Dilution	Dirichlet boundary	B.E.
		No flux	E.F. C.F.
	ALE	Prescribed deformation	E.F. C.F.
		Free deformation	B.E.

initial velocity of shielding gas is not zero in real manufacturing; however, it could be neglected in modeling supported by the following conclusions.

- Initial gas flow is about 10^{-1} m/s for real PBF-LB process [9]. Whereas the impact of initial gas flow on vapor induced flow is significant only when it is strong enough and beyond the threshold. This threshold is dependent on processing parameters and material properties. In PBF-LB of IN625, a parametric study of initial gas flow was performed and revealed that it has non-negligible impact on vapor plume if initial gas flow is larger than 6.7 m/s [26]. Although material properties have changed from IN625 to 316 L, the threshold for PBF-LB of 316 L is expected to be near 10 m/s because physical phenomena are similar for PBF-LB of IN625 and PBF-LB of 316 L. Therefore, initial gas flow of about 10^{-1} m/s is below the threshold and not considered due to its weak impact on vapor plume flow.
- According to the modeling and experimental results from this work, vapor plume flow and vapor-induced gas flow only act within 0.5 mm around the center of melt pool. Weak initial gas flow with lower velocity has little impact on melt pool dynamics, vapor-induced flow and the resulting powder entrainment.

Accordingly, initial gas flow is not included in this work.

Besides, the fluid flow inside the melt pool is Newtonian, laminar, and impressible, with the Boussinesq assumption. The energy distribution of the laser heat source is Gaussian. The mushy zone, in which the temperature is between solidus and liquidus, is treated as porous medium.

2.4. Modeling geometry and discretization

A 2D axisymmetric two-domain model, including substrate and gas domains, is developed, in which melt pool dynamics and gas kinetics are simulated, respectively. The details of model geometry and mesh discretization are illustrated in Fig. 2. In a typical simulation case, substrate and gas domains are discretized by unstructured triangular mesh with a maximum size of 35 μm. Especially, mesh at the domain boundary (boundary B.E.) is refined with the maximum size of 8 μm. The model geometry is finally discretized by 13,000 units.

2.5. Governing equations

Multiple physics fields are considered as the study focuses on both the melt pool behavior and vapor dynamics. Descriptions of governing equations are given as follows.

2.5.1. Substrate domain

The governing equations of mass, momentum, and energy conservation could be described as follows:

$$\nabla \bullet (\rho \mathbf{u}) = 0 \tag{1}$$

$$\rho \frac{\partial \boldsymbol{u}}{\partial t} + \rho(\mathbf{u} \bullet \nabla)\boldsymbol{u} = \nabla \bullet (\mu \nabla \boldsymbol{u}) - \nabla \boldsymbol{p} + \rho \boldsymbol{g} - A_{mush}\boldsymbol{u}(1-f_l)^2 / \left(f_l^3 + M\right) \tag{2}$$

$$\rho C_p^{eq} \frac{\partial T}{\partial t} + \rho C_p^{eq} \boldsymbol{u} \bullet \nabla T = \nabla \bullet (K \nabla T) + \rho \frac{\partial(\Delta H)}{\partial t} - \rho \boldsymbol{u} \nabla(\Delta H) \tag{3}$$

In the equations above, $\rho$is the density of the liquid metal. $\boldsymbol{u}$ denotes the velocity vector, and $\mu$is the dynamic viscosity. $\boldsymbol{p}$ and $\boldsymbol{g}$ represent the pressure and gravitational acceleration, respectively. A_{mush} denotes the restriction for fluid flow in mushy zone in which temperature is between solidus and liquidus. A_{mush} is assumed as a large constant and considered as $10^7 kg/m^3 \bullet s$ in the proposed model. f_l is the liquid phase fraction, which is 0 below solidus (T_s) and 1 above liquidus (T_l). Mathematically, it is described by $f_l = \frac{T-T_s}{T_l-T_s}$ when the temperature is between solidus and liquidus based on the Carmen-Kozeny relation [27]. M is a small

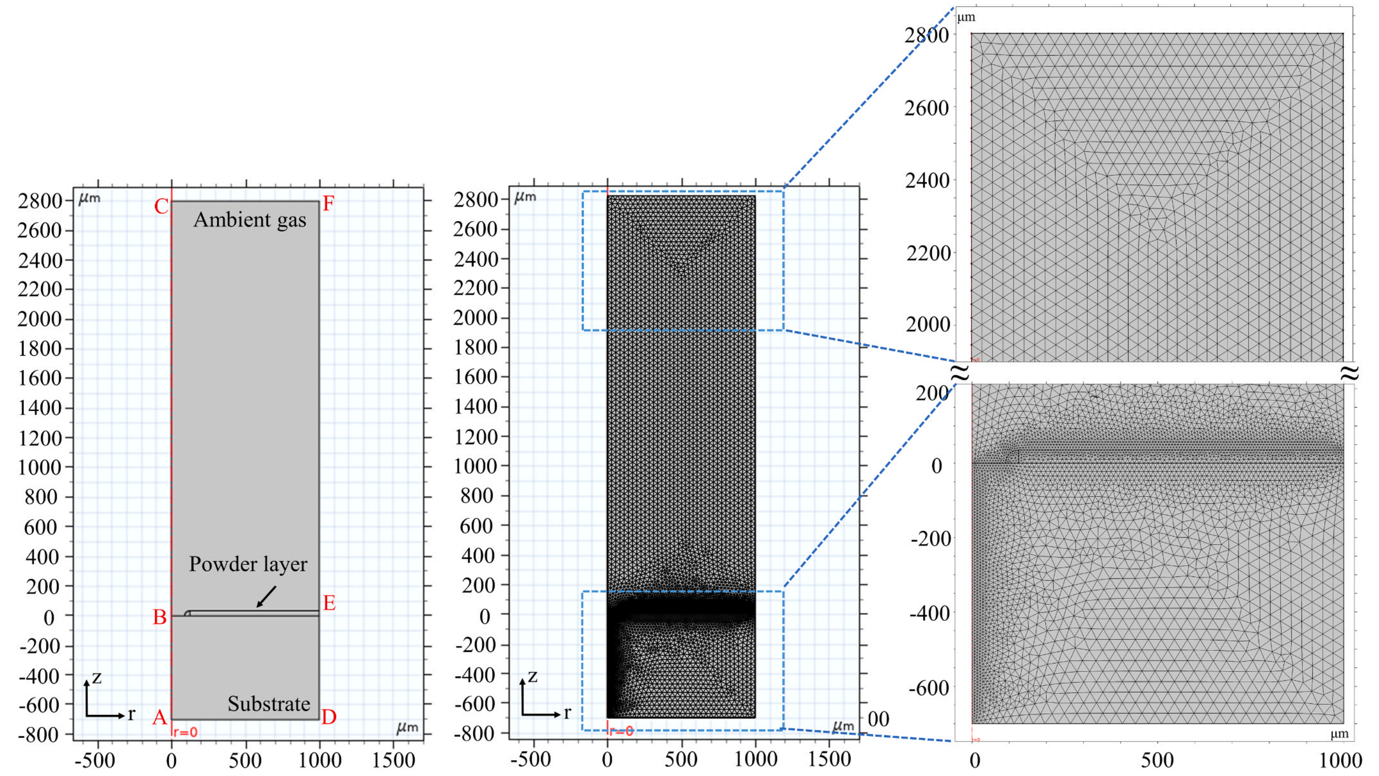

Fig. 2. Geometry and mesh discretization of the proposed Thermal-Fluid-Evaporation model.

constant and set to 10^{-4} to avoid numerical singularity. When the liquid fraction f_l is zero, the role of M is essential. T is the transient temperature inside the melt pool. C_p^{eq} represents the equivalent specific heat and described by:

$$C_p^{eq} = C_p + \frac{L_m}{\sqrt{\pi \Delta T^2}} \exp\left[-\frac{(T - T_m)^2}{\Delta T^2} \right] \tag{4}$$

where $\Delta T = (T_l - T_s)/2$ and $T_m = (T_l + T_s)/2$, representing the solidification interval and the melting temperature, respectively. Additionally, K is the thermal conductivity and $\Delta H = L_m f_l$ is the specific enthalpy caused by phase change, in which L_m and f_l are the enthalpy of fusion and fraction of liquid phase, respectively.

2.5.2. Gas domain

In the gas domain, heat transfer, dilution of vapor plume, coupled vapor plume flow, and vapor-induced gas flow with compressibility are all considered. Thus, the governing equations of Eq. (1), Eq. (2), and Eq. (3) are naturally considered and coupled in the modeling of the gas domain.

Besides, the dilution equation is also solved in the gas domain and can be given as follow:

$$\frac{\partial C_{plu}}{\partial t} + \boldsymbol{u} \bullet \nabla C_{plu} = \nabla \bullet (D \nabla C_{plu}) + S \tag{5}$$

In Eq. (5), C_{plu} is the fraction of vapor plume, which is considered as one phase. D is the diffusion coefficient and S is the source term. Because the magnitude of vapor plume flow is about 100 m/s, dilution of vapor plume at ambient gas is expected to be dominated by convection. Thus, D is treated as a constant because plume diffusion is not significant.

Especially, fluid flow at gas domain is compressible and the mixture of vapor plume and shielding gas is assumed as binary ideal gas. Mixture density can be calculated by:

$$\overline{\rho} = \frac{p \overline{M}}{RT} \tag{6}$$

where $\overline{M}$ is averaged molar mass, p is atmospheric pressure, and R is a universal gas constant. $\overline{M}$ is calculated by the following relation.

$$\overline{M} = C_{plu} M_{plu} + (1 - C_{plu}) M_{amb} \tag{7}$$

in which M_{plu} and M_{amb} are the molar mass of vapor plume and shielding gas, respectively.

2.6. Boundary conditions

Boundary conditions are essential for modeling accuracy. Physicl field, boundary condition and the corresponding location in model geometry are summarized in Table 2. The boundary I.D. listed in the table is illustrated in Fig. 2. Boundary A.B. and B.C. are the symmetry axis, thus set as symmetry boundary for all the physical fields in substrate and gas domains.

2.6.1. Energy boundary

The energy boundary at the gas/liquid surface (boundary B.E.) is given as:

$$-K\frac{\partial T}{\partial z} = (1 - R_\lambda)\cos\theta \frac{2P}{\pi {r_b}^2} \exp\left(-\frac{2r^2}{r_b^2} \right) - h_c (T - T_{ref}) - \sigma_b \varepsilon \left(T^4 - T_{ref}^4 \right) - \dot{m} L_v \tag{8}$$

In Eq. (8), the first term on the right hand is laser heat input. R_λ is the reflectivity of substrate. θ is the laser incident angle and varies with the deformation of gas/liquid surface. It should be noted that ray tracing of laser beam is not considered but the absorbed laser energy depends on both the reflectivity R_λ and incident angle θ. P is the laser power, r_b and r represent the effective laser radius and distance from the laser center, respectively. Moreover, the second term and third term denote the heat loss caused by heat convection and radiation, respectively. h_c represents the heat transfer coefficient of convection. σ_b denotes the Stefan-Boltzmann constant and ε is the emissivity. The last term represents the heat loss caused by material evaporation. $\dot{m}$ is the ablation rate and L_v is the enthalpy of evaporation.

Additionally, thermal continuity is assumed at the domain boundary (boundary B.E.).

$$T_{sub} = T_{gas} \tag{9}$$

Ablation rate, $\dot{m}$ is commonly described by the Hertz-Langmuir relation.

$$\dot{m} = (1-\beta_R)\sqrt{\frac{M_{plu}}{2\pi RT}}\quad P_{sat}(T) \tag{10}$$

in which β_R denotes the retro-diffusion coefficient, representing the fraction of vapor particles that re-condensate. M_{plu} is the molar mass of the vapor plume and P_{sat} is the statured vapor pressure. Here, the Clausius-Clapeyron law is introduced to calculate the vapor pressure.

$$P_{sat} = P_{atm}\exp\left[\frac{ML_v}{RT_V}\left(1-\frac{T_V}{T}\right)\right] \tag{11}$$

where P_{atm} is the pressure of ambient gas. T_V is the boiling temperature for substrate and assumed equal between P_{sat} and P_{atm} because it changes little.

In the proposed model, the boiling temperature of 316 L is 3100 K and much smaller than the peak temperature of 3650 K inside the melt pool. As a result, the vaporization intensity, characterized by β_R, is neither too low nor too high and could be thought of interim intensity. In this situation, some of the vapor powders are confined by shielding gas, while others with higher energy can expel the restriction from surrounding gas. For accurate modeling of metal evaporation with interim intensity, Pang et al. proposed the following numerical relation [28].

$$\dot{m} = \begin{cases} 0, & 0 < T < T_L \\ a_1T^3 + b_1T^2 + c_1T + d_1, & T_L < T < T_H \\ (1-\beta_R)\sqrt{\dfrac{M}{2\pi RT}}P_{sat}(T), & T > T_H \end{cases} \tag{12}$$

Threshold T_L and T_H respectively denote the low and high evaporation-intensity regimes corresponding to Pang's law. Vaporization intensity β_R is 0.18.

At the substrate domain, A.D. and D.E. are convection boundary. At gas domain, boundary C.F. and E.F. are considered as insulation.

2.6.2. Momentum boundary

Momentum condition at gas/liquid surface (boundary B.E.) could be expressed as:

$$[\nabla \bullet (\mu\nabla \boldsymbol{u}) - \nabla \boldsymbol{p}] \bullet \boldsymbol{n} = \sigma\kappa\boldsymbol{n} + \gamma\nabla_s T - (P_s - P_{atm}) \bullet \boldsymbol{n} \tag{13}$$

The first and second term at right hand represent capillary force and thermal capillary force, respectively. $\kappa$is the gas/liquid surface curvature. P_s is the recoil pressure induced by material evaporation and could be given by:

$$P_s = \begin{cases} P_{atm}, & 0 < T < T_L \\ a_2T^3 + b_2T^2 + c_2T + d_2, & T_L < T < T_H \\ \dfrac{1}{2}(1+\beta_R)P_{sat}(T), & T > T_H \end{cases} \tag{14}$$

Additionally, no-slip wall is used for boundary A.D. and D.E. at substrate domain. Pressure outlet is set for boundary E.F. and C.F. at gas domain.

2.6.3. Mass continuity

Especially, mass continuity at domain boundary (boundary B.E.) is considered.

$$\rho_L(\boldsymbol{u_L}\cdot\boldsymbol{n} - \boldsymbol{V_I}) = \rho_V(\boldsymbol{u_V}\cdot\boldsymbol{n} - \boldsymbol{V_I}) = .m^{\cdot} \tag{15}$$

where $\rho_L$and ρ_V represent the density for liquid phase and gas phase, respectively. $\dot{m}/\rho_L$ is the speed of liquid ablation front and not comparable to liquid recession speed $\boldsymbol{u_L} \bullet \boldsymbol{n}$. Thus,

$$\boldsymbol{V_I} = \boldsymbol{u_L} \bullet \boldsymbol{n} \tag{16}$$

Besides, $\dot{m}/\rho_V$ denotes the ejection speed of vapor powders at Knudsen layer and much larger than liquid recession speed. Therefore,

$$\boldsymbol{u_V}\cdot\boldsymbol{n} = .\boldsymbol{m}^{\cdot}/\boldsymbol{\rho_V} = \boldsymbol{V}_{inlet} \tag{17}$$

V_{inlet} is the inflow velocity at boundary B.E. for gas domain.

2.6.4. ALE boundary

Gas/liquid surface is captured by the ALE method. In detail, boundary B.E. is free deformation, indicating its displacement is not restricted. Besides, displacement along z direction is not allowed for boundaries A.D. and C.F., and displacement at r direction is also restricted for boundaries D.E. and E.F.

3. Results and discussion

3.1. Validation of thermal-fluid model

To validate the proposed computational model, the simulated cross-section of the fusion zone is compared with the experimentally obtained result [29]. As depicted in Fig. 3A, the simulated fusion line is consistent with the optical observation. A quantitative comparison is next performed using two significant dimensional definitions illustrated in Fig. 3B, i.e., half melt width and depth. In the present study, evaporation occurs at the gas/liquid surface, and a high-speed plume directly jets into shielding gas. The resulting recoil pressure from evaporation is much higher than ambient pressure, resulting in a keyhole due to its drilling effect [28]. The comparison in Fig. 3C shows that the simulated dimensions agree well with the experimentally observed results.

3.2. Laser-induced vapor plume flow and vapor-induced gas flow

Considering the impact of gas type and ambient pressure, melt pool dynamics and gas kinetics are directly coupled with the consideration of the dilution of high-concentration plumes. As illustrated in Fig. 1, powder entrainment can be classified as powder spattering and denudation. The causal relation between spattering, denudation, vapor plume flow, and vapor-induced gas flow will be numerically and experimentally analyzed in PBF-LB for 316 L powders. The processing parameters in this section can be listed as follows: shielding gas pressure of 1 atm and 0.05 atm, laser power of 312 W, and laser radius of 100 μm. Vapor plume flow and vapor-induced gas flow in 1 atm argon and 1 atm helium are depicted in Fig. 4. As shown, the velocity of vapor plume flow generated from the Knudsen layer [28] is up to ~200 m/s. The calculated Mach number, representing the ratio of characteristic speed to the speed of sound at the surrounding medium, is over 0.7; thus, gas compressibility should be included. Additionally, vapor-induced gas flow is about 10 m/s, and its velocity is much smaller than vapor plume flow. High-speed plume jets into shielding gas at subsonic speed and is quickly diluted within several millimeters, which agrees well with the experimental observations in [3]. With the permanent time interval of 20 μs, the travel distance of the plume head increases from Fig. 4A to Fig. 4B to Fig. 4C, indicating that the vapor plume travels faster with processing going on. Interestingly, the morphology of the vapor plume characterized by mushroom head and conical-structure core area with the plume concentration over 60 % changes little from Fig. 4A to Fig. 4C,

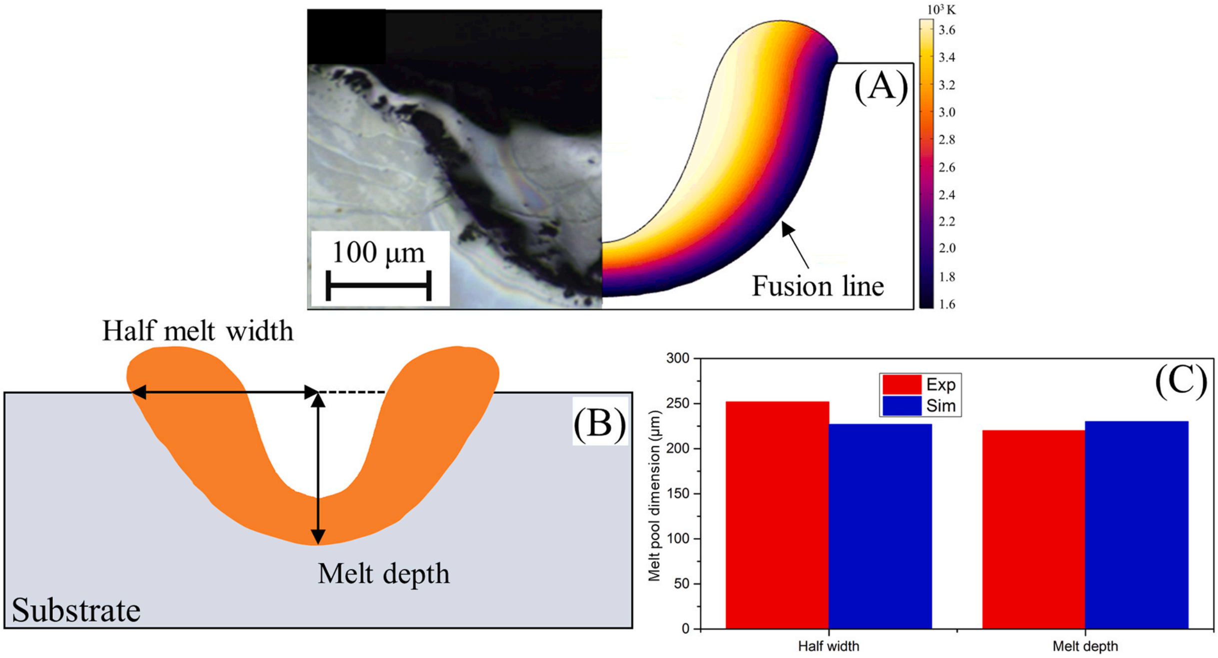

Fig. 3. Validation of the proposed computational model. (A) Comparison of melt pool morphology between experimental observation [29] and simulated result. (B) Schematic sketch of the melt pool in keyhole mode and the dimension definition. (C) Quantitative validation of experimentally observed and calculated dimensions. Material: IN625; Parameters: laser power of 700 W, laser radius of 102.5 µm, and pulse duration time of 3 ms.

which is attributed to the strong restriction from shielding gas.

It has been experimentally demonstrated that the impact of gas type on vapor-induced flow and powder entrainment is significant [8]; thus, modeling in 1 atm helium, which is 10x lighter than argon, is also performed. Compared with 1 atm argon, vapor plume flow is at the same magnitude, and plume morphology is similar in 1 atm helium with a mushroom head and conical-structure core area. But the vapor plume travels a much longer distance in helium, indicating the viscous restriction for the vapor plume is smaller due to its smaller density. In the Schlieren imaging observation conducted by Baehr et al. [21], the laser-induced plume is also observed reduced when He or He-containing shielding gas is employed. Besides, it is interesting that the peak velocity of vapor plume flow observed in the high-concentration area (>90 %) is equal though shielding gas changes from argon to helium. This is because the vapor plume flow of high-concenrtation area is littely affected by the shielding gas. The feature of the high-concentration area also supports this conclusion because the shape in 1 atm argon is similar to that 1 atm helium as shown in Fig. 4.

For further analysis of vapor-induced gas flow, the velocity distribution near the powder layer surface in 1 atm argon and 1 atm helium are plotted in Fig. 5A and Fig. 5B, respectively. The negative sign for the labeled velocity denotes that gas flows toward the melt pool. As depicted, vapor-induced gas flow increases towards the melt pool, whereas it is 3 times larger in 1 atm helium. The maximum velocity is about 10 m/s in 1 atm argon, while 30 m/s for 1 atm helium. Vapor-induced gas flow is driven by vapor-induced shear stress. Accordingly, it increases towards the melt pool because the driving force, i.e., the shear stress between high-speed plume and shielding gas, is larger near the melt pool. For the 3 times larger velocity in 1 atm helium, 10 times lighter relative atomic mass may be the major contributor. Besides, it can also be observed that vapor-induced gas flow is weak far away from the melt pool (r > 150 µm), and only acts in a small area from r = 50 µm to r = 150 µm.

The drag force of vapor-induced flow for powder entrainment is analyzed here. Drag force F_d is described by $F_d = 0.5\rho_{gas}C_xSU^2$ [30], in which ρ_{gas} is gas density, C_x is drag coefficient, S is the projected area of powder, and U is the characteristic velocity. In the present study, U is denoted by the maximum velocity. In detail, $C_x = 18.5/\mathrm{Re}^{0.6}$, where R_e is Reynolds number. Non-dimensional number R_e expresses the ratio of inertial force to viscous force and it is expressed by $R_e = \rho UL/\mu$, in which L is the characteristic length and μ is dynamic viscosity. Consequently, the final relation can be expressed by $F_d = 0.5\rho_{gas}^{0.4}\frac{L^{1.4}}{4}\mu^{0.6}U^{1.4}$. From argon to helium, the gas properties and velocity field have significantly differed, thus, the driving force is expected to change. For the powder spattering shown in the insets of Fig. 5, many spatters are observed in 1 atm argon, while no spatter is found in 1 atm helium. In addition, the vapor plume travels a much longer distance in 1 atm helium, consistent with the simulated result in Fig. 4. Based on the obtained relation of drag force, the ratio of the drag force for powder spattering in 1 atm argon to the drag force for powder spattering in 1 atm helium can be expressed by $R_{spat} = \rho_{Ar}^{0.4}\mu_{Ar}^{0.6}U_{Ar}^{1.4}/\rho_{He}^{0.4}\mu_{He}^{0.6}U_{He}^{1.4}$. Based on the properties in Table 1 and the calculated velocity of vapor plume flow, the final R_{spat} is 2.72. Pauzon et al. [22,23] also confirm that the existing of He in the shielding gas contributes to the reduction of powder spatter.

For powder denudation, it is experimentally observed that the denudated is greater in helium [8]. This phenomenon could also be explained by the calculated drag force from the simulated gas flow. In detail, the ratio of the drag force for powder denudation in 1 atm argon to the drag force for powder denudation in 1 atm helium can be calculated by $R_{denu} = \rho_{Ar}^{0.4}\mu_{Ar}^{0.6}U_{Ar}^{1.4}/\rho_{He}^{0.4}\mu_{He}^{0.6}U_{He}^{1.4}$. Based on the properties in Table 1 and the calculated velocity for shielding gas flow, the final R_{denu} is 0.582. Therefore, the drag force is stronger and the powder denudation area is greater in helium. Accordingly, it could be further concluded that drag force from vapor-induced gas flow is the main contributor to powder denudation. For powder spattering, it could be concluded that the drag force from vapor plume flow is the main driving factor. Firstly, as shown in the insets of Fig. 5, spatters distribute around the plume head while powder denudation is found at the region where vapor-induced gas flow acts. Besides, under the same processing conditions, the ratio of the drag force generated by vapor-plume flow to that induced by vapor-induced gas flow can be evaluated by $R_{plume/gas}=U_{plume}^{1.4}/U_{gas}^{1.4}$. Obviously, vapor plume flow (200 m/s) is much

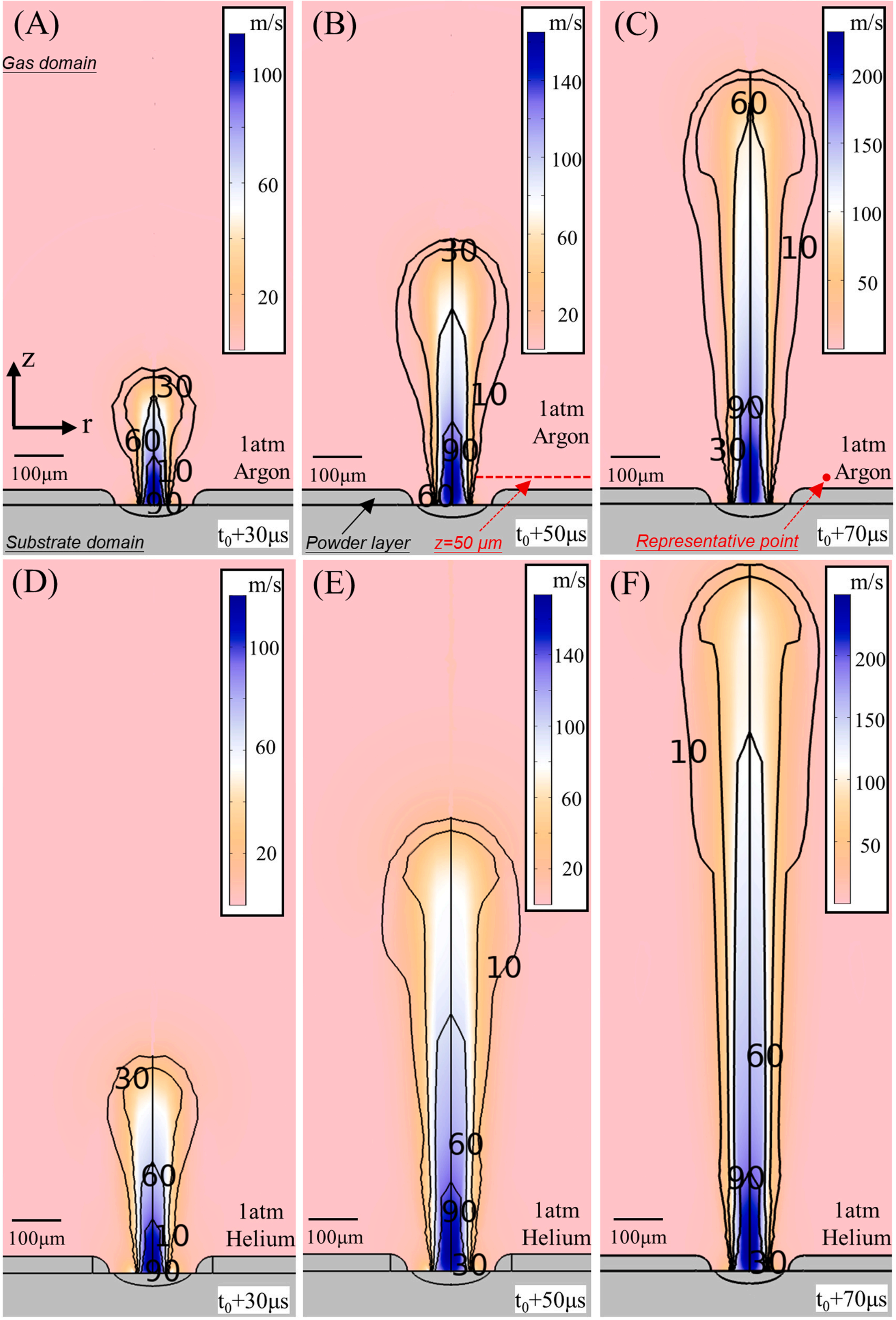

Fig. 4. Color contour represents the velocity distribution of vapor plume flow and vapor-induced gas flow during PBF-LB of 316 L powders. The isoline denotes the mass fraction of the vapor plume. Four concentration levels are labeled along the decreasing direction from the plume core to the plume boundary, i.e., 90 %, 60 %, 30 %, and 10 %, respectively. $t_0 = 372$ μs corresponding to the beginning of evaporation. Fig. 4A, Fig. 4B, and Fig. 4C show the velocity distribution of vapor plume flow and vapor-induced gas flow, and the mass fraction of vapor plume in 1 atm argon at $t_0 + 30$ μs, $t_0 + 50$ μs, and $t_0 + 70$ μs, respectively. Fig. 4D, Fig. 4E, and Fig. 4F show the velocity distribution of vapor plume flow and vapor-induced gas flow, and the mass fraction of vapor plume in 1 atm helium at $t_0 + 30$ μs, $t_0 + 50$ μs, and $t_0 + 70$ μs, respectively.

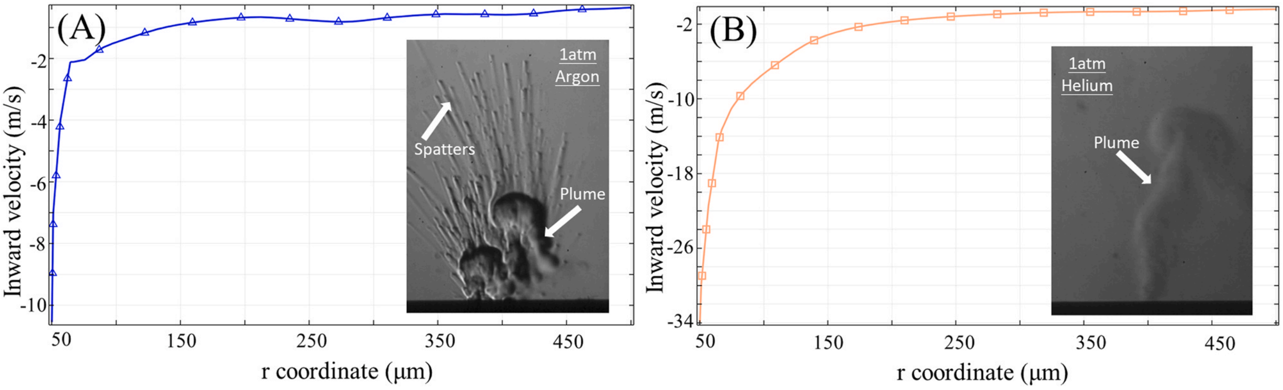

Fig. 5. Line graphs in Fig. 5A and Fig. 5B show the velocity distribution of vapor-induced gas flow at z = 50 μm (see Fig. 4) in 1 atm argon and 1 atm helium, respectively. Insets of experimentally observed spatters and plumes are from [8].

superior to vapor-induced gas flow (10 m/s), resulting in a much greater drag force. Thirdly, vapor-plume flow acts within ~ one milimeter directly above the melt pool, while the vapor-induced gas flow acts the areas away from melt pool and flows towards melt pool.

In summary, plume morphology is similar in 1 atm argon and 1 atm helium with mushroom head and conical-structure core area, but vapor plume travels a much longer distance in 1 atm helium. More spatters are observed in 1 atm argon, while the powder denudation in 1 atm helium is greater due to the higher drag force. Vapor plume flow results in powder spattering with much higher speed, while vapor-induced gas flow significantly contributes to powder denudation with lower speed.

The gas type has a significant impact on vapor-induced flow and powder entrainment. Moreover, ambient pressure is also experimentally proved non-negligible [8]. Consequently, vapor-induced flow in 0.05 atm argon is next modeled in Fig. 6 and compared with the results in 1 atm argon shown from Fig. 4A to Fig. 4C. There are significant differences of gas kinetics induced by ambient pressure when it varies from 1 atm to 0.05 atm. In 0.05 atm argon, a vapor plume with a mushroom head and conical-structure core is also observed; however, it travels a much smaller distance, and the width of the plume head increases 2 times. Viscous restriction for vapor plume flow is much smaller because ambient pressure (0.05 atm) is only one-twentieth of the original pressure (1 atm). Therefore, it results in a smaller travel distance and wider plume head in 0.05 atm. In addition, the peak velocity of vapor plume flow increases to 500 m/s, which is two times larger than that in 1 atm argon. Vapor-induced gas flow will also change with ambient pressure because it is driven by the shear stress between the vapor plume and shielding gas. For example, the peak velocity of vapor-induced gas flow at the representative point (see Fig. 4C and Fig. 6C) is 1 m/s for 0.05 atm argon and 5 m/s for 1 atm argon at 422 μs. As a result, denudation is expected to be attenuated in 0.05 atm due to the weaker vapor-induced gas flow, which means the smaller driving force. In conclusion, when ambient pressure decreases from 1 atm to 0.05 atm, vapor plume flow is stronger but travles a much smaller distance, while the vapor-induced gas flow is weaker.

3.3. Applications to PBF-LB

Fundamental conclusions obtained from the modeling of vapor-induced flow will be promoted in PBF-LB to probe potential approaches to mitigate spattering and denudation, then achieve the quality improvement of as-built parts. Powder spattering and denudation in 1 atm argon and 0.05 atm argon observed by the in-situ X-ray device in ANL are respectively shown in Fig. 7. Spatters and denudated powders are highlighted by the yellow and blue circles, respectively. The divergence angle for spattering is shown by the solid red arrow. It should be

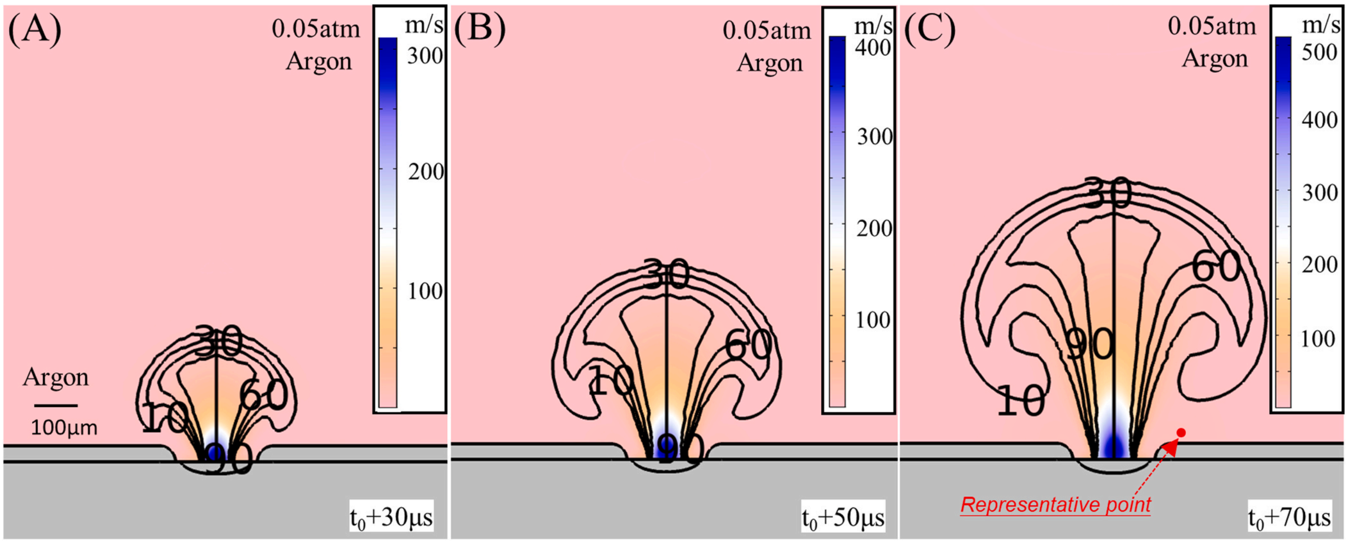

Fig. 6. Color contour denotes velocity distribution of vapor plume flow and vapor-induced gas flow during PBF-LB of 316 L powders. The isoline indicates the mass fraction of the plume. Four concentration levels are labeled along the decreasing direction from the plume core to the plume boundary, i.e., 90 %, 60 %, 30 %, and 10 %, respectively. t_0 = 372 μs corresponding to the beginning of evaporation. Fig. 6A, Fig. 6B, and Fig. 6C show the velocity field of vapor plume flow and vapor-induced gas flow, and the mass fraction of vapor plume in 0.05 atm argon at $t_0 + 30$ μs, $t_0 + 50$ μs, and $t_0 + 70$ μs, respectively.

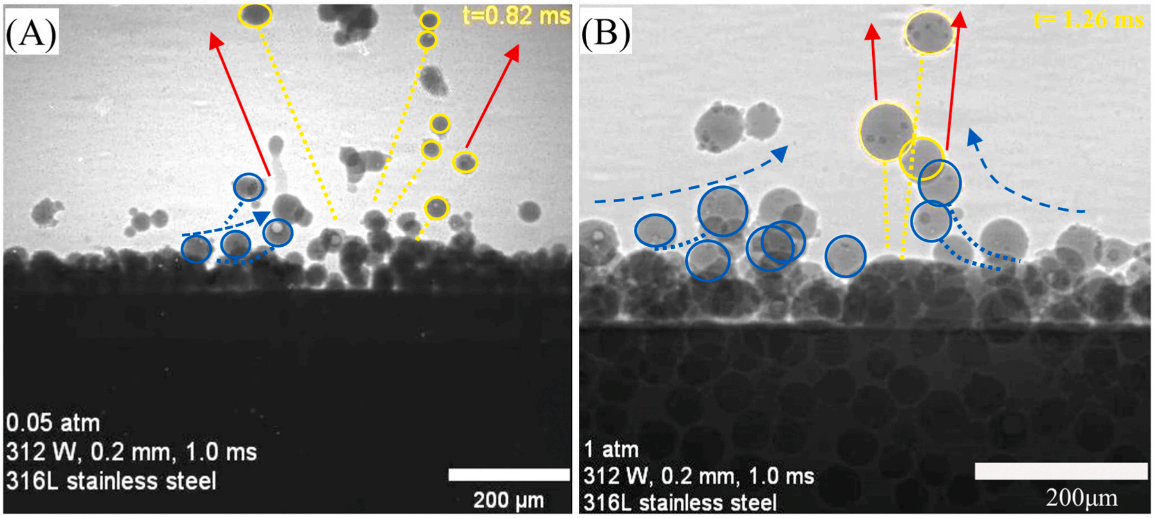

Fig. 7. In-situ observation of power spattering and denudation during PBF-LB of 316 L powders. (A) X-ray image showing spattering and denudation in 0.05 atm argon. (B) X-ray image showing spattering and denudation in 1 atm argon. X-ray images are taken from the supplementary videos of [7]. Parameters for PBF-LB experiments are same to these in Section 3.2.

noted that the powders in Fig. 7A and Fig. 7B are the same, and the difference in visualized dimension has resulted from the change of scale bar. As depicted, the number of spatters increases, and divergence angle is larger in 0.05 atm argon because the vapor plume flow, the dominant driver for spattering, is stronger in lower pressure. Nevertheless, more denudated powders towards the melt pool are observed in 1 atm argon because the vapor-induced flow is stronger in higher pressure, resulting in a larger drag force. When the helium pressure is higher, the reduction of powder spattering and the greater denudation are also found by Schlieren imaging [8,32]. It confirms that the conclusions on the powder entrainment versus ambient pressure remains the same though the gas type changes.

Based on the above-mentioned numerical and experimental investigations, and also inspired by previously published insightful studies focused on powder dynamics, a clear schematic sketch aimed at illustrating the causal mechanisms of vapor-induced flow and powder entrainment during PBF-LB is thus constructed and plotted in Fig. 8. As shown, horizontal axis expresses the variation of gas type, i.e., two widely used shielding gas in PBF-LB: argon and helium, as well as its impact on gas kinetics and the resulting spattering and denudation. In contrast, the vertical axis depicts the impact of ambient pressure on vapor-induced flow and powder entrainment. It is worth noting that the following discussions of vapor plume flow and vapor-induced gas flow are supported by the obtained modeling conclusions and in-situ

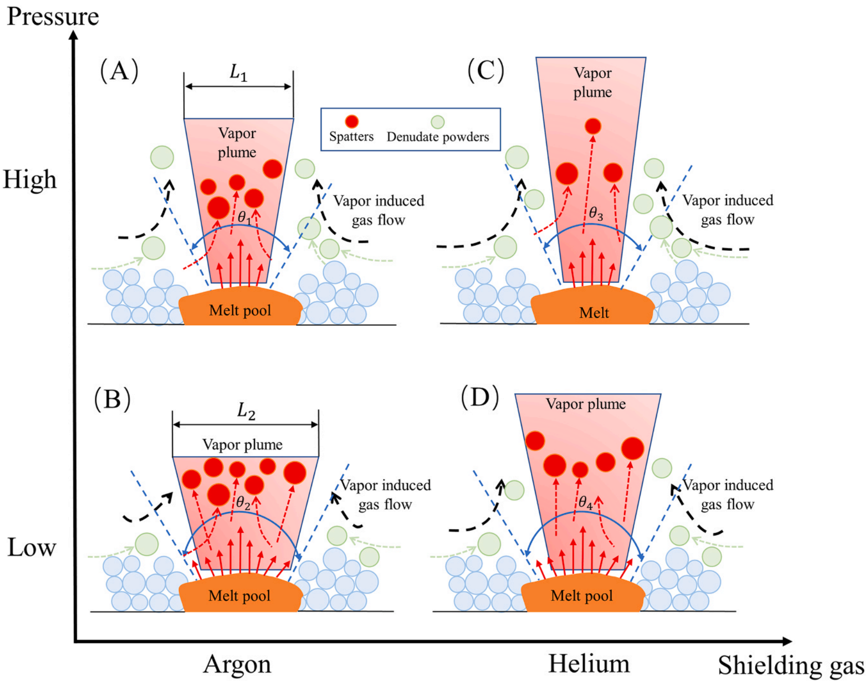

Fig. 8. Schematic sketch showing the causal mechanisms of vapor-induced flow and powder entrainment considering the variation of ambient pressure and shielding gas type. Schematics along the horizontal axis show the vapor-induced flow and powder entrainment versus gas type, i.e., argon and helium. Schematics along the vertical axis show the impact of ambient pressure on vapor-induced flow and powder entrainment. (A) Vapor plume jets into shielding gas, and vapor-induced gas flow is driven by the shear stress between the vapor plume and shielding gas. Vapor plume flow results in powder spattering, while the vapor-induced gas flow causes powder denudation. The solid red arrows and solid black arrows represent the impact of vapor plume flow and vapor-induced gas flow, respectively. The length of the arrows denotes relative intensity. Red and blue circles are the spatters and denudated powders, respectively. The red and blue arrows are the trajectories of spatters and denudated powders, respectively. (B) Wider vapor plume with higher speed, weaker vapor-induced gas flow, more spatters, and less denudated powders in lower environmental pressure. $L_1 < L_2$ are the width of plume head. $\theta_1 < \theta_2$ are the divergence angle [31], and they increase as ambient pressure drops. (C) When shielding gas changes from 1 atm argon to 1 atm helium, the vapor plume travels a much longer distance with similar morphology and equal speed. Vapor-induced gas flow is stronger in helium and results in greater powder denudation. Together, less spatters are generated in helium. (D) The changes in vapor plume flow, vapor-induced gas flow, spattering, and denudation from 1 atm helium to 0.05 atm helium are similar to those from 1 atm argon to 0.05 atm argon.

experimental observations. Whereas, the discussions of powder entrainment are not directly obtained from modeling, but hypothesis mechanisms supported by the fact that powder spattering, and denudation are significantly driven by vapor plume flow and vapor-induced gas flow, respectively, though the experimental results could also help illustrate. The direct observations in Fig. 7 confirms the modeling findings versues abmbient pressure, and the discussions in term of gas tepy, i.e., argon and helium, are supported by the experimental observation through in-situ technologies [21–23]. For example, the more rapid expansion of the vapor plume and the reduction of powder spattering have been observed by X-ray diffraction observation in pure helium or He-containing atmosphere [22,23].

Under lower ambient pressure, as shown in Fig. 8B and Fig. 8D, the vapor plume is easily diluted with a wider head and higher velocity. As a result, more spatters are generated with a larger divergence angle, as illustrated by θ_2 in Fig. 8B and θ_4 in Fig. 8D. The number of spatters increases with the decrease of ambient pressure, which is adjustable in experiment and modeling. Conversely, vapor-induced gas flow is stronger, and more powders will be denudated towards the melt pool under higher pressure. In contrast, when the ambient pressure is constant, the vapor plume travels a longer distance while the number of spatters decreases in helium, as illustrated in Fig. 8A and C. The change in divergence angle is not significant, however, powder denudation is recorded to be greater in helium as the drag force is stronger in helium. Based on the study, it is suggested that the modulation of ambient pressure and the right choice of ambient gas could help mitigate powder spattering and denudation. Therefore the controlled spattering and denudation will help reducing the defects in PBF-LB including lack of fusion, melting/solidified spatters, and unexpected pores; subsequently improving the quality of additively manufactured parts.

4. Conclusion

An improved transient Thermal-Fluid-Evaporation model coupling melt pool dynamics and gas kinetics is developed to analyze the vapor-induced flow and the resulting powder entrainment during PBF-LB. In-situ observations including X-ray and Schlieren imaging in the current study are reused from the literatur to assist the investigation. Fundamental conclusions could be summarized as follows.

(1) In 1 atm argon, a vapor plume is directly generated from the melt pool. The velocity magnitude is up to ~ 200 m/s with mushroom head and conical-structure core area (plume concentration >60 %). Vapor-induced gas flow is driven by the shear stress between the vapor plume and shielding gas, and its velocity magnitude is about 10 m/s.

(2) In 1 atm helium, the peak velocity of vapor plume is around 200 m/s with the same structure as that in 1 atm argon, but it travels a much longer distance and is diluted faster. The peak velocity of vapor-induced gas flow increases to 30 mm/s in 1 atm helium as its relative atomic mass is much smaller.

(3) Vapor-plume flow acts within ~ one milimeter directly above the melt pool, while the vapor-induced gas flow acts at the areas away from melt pool and flows towards melt pool. The drag force for powder entrainment generated by vapor-plume flow is much greater than that from vapor-induced gas flow. The spatters are found around plume head but the denudation is observed at the region where vapor-inudced gas flow occurs. It is further concluded that vapor plume flow significantly results in powder spattering with much higher speed , while the vapor-induced gas flow is the main contributor to powder denudation with lower speed.

(4) In 1 atm argon, more spatters are observed because the drag force for spattering is 2.72 times larger in 1 atm argon, but the powder denudation is greater in 1 atm helium as the ratio of drag force for denudation in 1 atm argon to that in 1 atm helium is only 0.582.

(5) The vapor plume induces more spatters in 0.05 atm argon as the plume is diluted faster with a twofold wider plume head and the two times higher peak velocity as a result of the pressure drop-induced significant reduction of viscosity restriction. The divergency angle in 0.05 atm argon is larger than that in 1 atm argon for the weaker restriction and faster dilution. Therefore, higher ambient pressure and helium as the shielding gas are potential approaches to mitigate spattering and denudation in PBF-LB.

Declaration of Competing Interest

All the authors declare that there is no conflict of interest.

Data availability

Data will be made available on request.

Acknowledgements

The computational work is performed at Northwestern University while Zhiyong Li was a visiting scholar. The financial supports from National Natural Science Foundation of China (No. 12202448) and the Chinese Scholarship Council (CSC) are acknowledged by Zhiyong Li. Zhengtao Gan and Wing Kam Liu are grateful for the support of the US NSF grant CMMI-1934367. All the authors thank Abdullah Al Amin in Northwestern University for the help on editing.

References

[1] A. De, W. Zhang, Additive manufacturing of metallic components–process, structure and properties, Prog. Mater. Sci. 92 (2018) 112–224.
[2] L.Y. Chen, J.Q. Xu, H. Choi, H. Konishi, S. Jin, X.C. Li, Rapid control of phase growth by nanoparticles, Nat. Commun. 5 (2014) 3879.
[3] Y.A. Mayi, M. Dal, P. Peyre, M. Bellet, C. Metton, C. Moriconi, R. Fabbro, Laser-induced plume investigated by finite element modelling and scaling of particle entrainment in laser powder bed fusion, J. Phys. D: Appl. Phys. 53 (2020), 075306.
[4] J. Zhu, H. Zhou, C. Wang, L. Zhou, S. Yuan, W. Zang, A review of topology optimization for additive manufacturing: Status and challenges, Chin. J. Aeronaut. 3 (4) (2021) 91–110.
[5] Y. Liu, Y. Yang, S. Mai, D. Wang, C. Song, Investigation into spatter behavior during selective laser melting of AISI 316L stainless steel powder, Mater. Des. 87 (2015) 797–806.
[6] M. Taheri Andani, R. Dehghani, M.R. Karamooz-Ravari, R. Mirzaeifar, J. Ni, Spatter formation in selective laser melting process using multi-laser technology, Mater. Des. 131 (2017) 460–469.
[7] Q.L. Guo, C. Zhao, Luis I. Escano, Z. Young, Lh Xiong, K. Fezzaa, W. Everhart, B. Brown, T. Sun, L.Y. Chen, Transient dynamics of powder spattering in laser powder bed fusion additive manufacturing process revealed by in-situ high-speed high-energy x-ray imaging, Acta Mater. 151 (2018) 169–180.
[8] P. Bidare, I. Bitharas, R.M. Ward, M.M. Attallah, A.J. Moore, Laser powder bed fusion in high-pressure atmospheres, Int. J. Adv. Manuf. Technol. 99 (2018) 543–555.
[9] V. Gunenthiram, P. Peyre, M. Schneider, M. Dal, F. Coste, I. Koutiri, R. Fabbro, Experimental analysis of spatter generation and melt-pool behavior during the powder bed laser beam melting process, J. Mater. Process. Technol. 251 (2018) 376–386.
[10] H. Krauss, T. Zeugner, M.F. Zaeh, Layerwise monitoring of the selective laser melting process by thermography, Phys. Procedia 56 (2014) 64–71.
[11] T.G. Spears, S.A. Gold, In-process sensing in selective laser melting (SLM) additive manufacturing, Integr. Mater. Manuf. Innov. 5 (2016) 1–25.
[12] A. Wegner G. Witt Process Monitoring in Laser Sintering Using Thermal Imaging Repositories.lib.utexas.edu. 2011.
[13] M.A. Stokes, S.A. Khairallah, A.N. Volkov, A.M. Rubenchik, Fundamental physics effects of background gas species and pressure on vapor plume structure and spatter entrainment in laser melting, Addit. Manuf. 55 (2022), 102819.
[14] A. Masmoudi, R. Bolot, C. Coddet, Investigation of the laser-powder-atmosphere interaction zone during the selective laser melting process, J. Mater. Process. Technol. 225 (2015) 122–132.
[15] M.J. Matthews, G. Guss, S. A.Khairallah, A.M. .Rubenchik, P. J.Depond, W.E. King, Denudation of metal powder layers in laser powder bed fusion processes, Acta Mater. 114 (2016) 33–42.
[16] H. Chen, W.T. Yan, Spattering and denudation in laser powder bed fusion process: multiphase flow modelling, Acta Mater. 196 (2020) 154–167.
[17] K.C. Mills, Recommended values of thermophysical properties for selected commercial alloys. Cambridge. MA, Woodhead Publishing Limited,, 2002.

[18] Z.Y. Li, G. Yu, X.,L. He, S.X. Li, C.X. Tian, B.X. Dong, Analysis of surface tension driven flow and solidification behavior in laser linear welding of stainless steel, Opt. Laser Technol. 123 (2020), 105914.

[19] Z.T. Gan, Y.P. Lian, S.E. Lin, K.K. Jones, W.K. Liu, G.J. Wagner, Benchmark study of thermal behavior, surface Topography, and dendritic microstructure in selective laser melting of Inconel 625, Integr. Mater. Manuf. Innov. 8 (2019) 178–193.

[20] Z.K. Wang, W.T. Yan, W.K. Liu, M.B. Liu, Powder-scale multi-physics modeling of multi-layer multi-track selective laser melting with sharp interface capturing method, Comput. Mech. 63 (4) (2019) 649–661.

[21] S. Baehr, L. Melzig, D. Bauer, T. Ammann, M.F. Zaeh, Investigations of process by-products by means of Schlieren imaging during the powder bed fusion of metals using a laser beam, J. Laser Appl. 34 (2022), 042045.

[22] C. Pauzon, S.V. Petegem, E. Hryha, C.S.T. Chang, S. Hocine, H.V. Swygenhoven, C. Formanoir, S. Dubiez-Le, Goffd. Effect of helium as process gas on laser powder bed fusion of Ti-6Al-4V studied with operando diffraction and radiography, Eur. J. Mater. 2 (1) (2022) 422–435.

[23] C. Pauzona, B. Hoppeb, T. Pichlerc, S. Dubiez-Le Goffd, P. Forêtd, T. Nguyend, E. Hryha, Reduction of incandescent spatter with helium addition to the process gas during laser powder bed fusion of Ti-6Al-4V, CIRP J. Manuf. Sci. Technol. 35 (2021) 371–378.

[24] Z.Y. Mu, X. Chen, Z.C. Zheng, A.G. Huang, S.Y.Pang Laser, cooling arc plasma effect in laser-arc hybrid welding of 316L stainless steel, Int. J. Heat. Mass Transf. 132 (2019) 861–870.

[25] D.R. Lide, CRC Handbook of Chemistry and Physics, CRC Press,, Boca Raton, FL, 2003.

[26] D.C. Deisenroth, J. Neira, J. Weaver, H. Yeung. Effects of shield gas flow on melt pool variability and signature in scanned laser melting. Proceedings of the ASME 2020, 15th International Manufacturing Science and Engineering Conference, Cincinnati, OH, USA.

[27] V.R. Voller, C. Prakash, A fixed grid numerical modelling methodology for convection– diffusion mushy region phase-change problems, Int. J. Heat. Mass Transf. 30 (8) (1987) 1709–1719.

[28] S.Y. Pang, K. Hirano, R. Fabbro, T. Jiang, Explanation of penetration depth variation during laser welding under variable ambient pressure, J. Laser Appl. 27 (2015), 022007.

[29] Y.A. Mayi M. Dal P. Peyre M. Bellet C. Metton C. Moriconi R. Fabbro A Mesoscopic Approach for Modelling Laser Beam Melting (LBM) Sim-AM-2019, Pavia, Italy.

[30] S. Dey, A. Papanicolaou, Sediment threshold under stream flow: a state-of-the-art review, KSCE J. Civ. Eng. 12 (2008) 45–60.

[31] J. Yin, D.Z. Wang, L.L. Yang, H.L. Wei, P. Dong, L.D. Ke, G.Q. Wang, H.H. Zhu, X. Y. Zeng, Correlation between forming quality and spatter dynamics in laser powder bed fusion, Addit. Manuf. 31 (2020), 100958.

[32] P. Bidare, I. Bitharas, R.M. Ward, M.M. Attallah, A.J. Moore, Fluid and particle dynamics in laser powder bed fusion, Acta Mater. 142 (2018) 107–120.